Article

High-Resolution Real-Time Coastline Detection Using GNSS RTK, Optical, and Thermal SfM Photogrammetric Data in the Po River Delta, Italy

Massimo Fabris [1,*], Mirco Balin [2] and Michele Monego [1]

1 Department of Civil, Environmental and Architectural Engineering, University of Padua, 35131 Padua, Italy; michele.monego@unipd.it
2 Brenta Lavori srl, 35010 Vigonza, Italy; mircobalin@gmail.com
* Correspondence: massimo.fabris@unipd.it

Abstract: High-resolution coastline detection and monitoring are challenging on a global scale, especially in flat areas where natural events, sea level rise, and anthropic activities constantly modify the coastal environment. While the coastline related to the 0-level contour line can be extracted from accurate Digital Terrain Models (DTMs), the detection of the real-time, instantaneous coastline, especially at low tide, is a challenge that warrants further study and evaluation. In order to investigate an efficient combination of methods that allows to contribute to the knowledge in this field, this work uses topographic total station measurements, Global Navigation Satellite System Real-Time Kinematic (GNSS RTK) technique, and the Structure from Motion (SfM) approach (using a low-cost drone equipped with optical and thermal cameras). All the data were acquired at the beginning of 2022 and refer to the areas of Boccasette and Barricata, in the Po River Delta (Northeastern of Italy). The real-time coastline obtained from the GNSS data was validated using the topographic total station measurements; the correspondent polylines obtained from the photogrammetric data (using both automatic extraction and manual restitutions by visual inspection of orhophotos) were compared with the GNSS data to evaluate the performances of the different techniques. The results provided good agreement between the real-time coastlines obtained from different approaches. However, using the optical images, the accuracy was strictly connected with the radiometric changes in the photos and using thermal images, both manual and automatic polylines provided differences in the order of 1–2 m. Multi-temporal comparison of the 0-level coastline with those obtained from a LiDAR survey performed in 2018 provided the detection of the erosion and accretion areas in the period 2018–2022. The investigation on the two case studies showed a better accuracy of the GNSS RTK method in the real-time coastline detection. It can be considered as reliable ground-truth reference for the evaluation of the photogrammetric coastlines. While GNSS RTK proved to be more productive and efficient, optical and thermal SfM provided better results in terms of morphological completeness of the data.

Keywords: GNSS RTK; optical and thermal images; SfM photogrammetry; real-time coastline; Po River Delta; automatic extraction; multi-temporal comparison

1. Introduction

Coastal areas are a highly dynamic and complex environment, hosting approximately 10% and 44% of the Earth's population at elevations of 0–10 m and up to 150 km from the coast, respectively. The population density in these areas is expected to increase by 25% by 2050 [1]. These areas, characterized by significant socio-economic activities, are continuously exposed to natural risks (storms, storm surges, cyclones, hurricanes, extreme precipitation, and flooding) and sea level rise generated by climate change [2–4]. In many areas, mainly in river deltas, these effects are exacerbated by land subsidence [5–7].

These challenging environments are characterized by large topographic changes, differences in bed cover (rough surfaces alternating with textureless and reflective surfaces), the presence of water as channels, thin patches and deeper puddles, variations in the coastline due to the combined effects of human activities on land and sea, regional environmental modification, and climate change. All these effects can represent important challenging aspects for the monitoring of these areas [8].

Many studies were conducted by different researchers in the field of high-resolution deformations monitoring in coastal areas due to erosion and accretion phenomena. Structure from Motion (SfM) photogrammetry, LiDAR (Light Detection And Ranging), and Global Navigation Satellite System (GNSS) techniques were used to extract high-resolution and high-precision digital terrain models (DTMs). The comparison between these data acquired at different times and co-registered in the same reference system provided the areas and volumes involved in the deformation processes. In particular, for coastal areas, erosion and/or accretion can be measured by comparing the 0-level contour lines extracted from the DTMs [9–11].

In this context, the high-resolution coastline identification becomes a crucial challenge when analyzing flat areas. Reconstructing past coastlines can be achieved by using archival data: cartographies, aerial photogrammetry, and satellite imagery [12,13]. In many cases, more so for historical data, georeferenced digital models cannot be obtained due to the absence of Ground Control Points (GCPs) coeval with the past surveys and/or the lack of information about the tidal level when images were acquired. In these cases, the restitution can be performed directly on 2D orthophotomaps where the unknown tide level, with the water that can cover large portions when flat areas are involved, can have a very negative impact on the result of the real coastline [14].

The extraction of coastline from optical images can be performed automatically by means of various methods developed in recent decades. Supervised [15] and unsupervised [16,17] image classification methods, specific tools (Automatic Coastal Extraction Tool [18]) and suitable indices [19] can be used. In the latter approach, many indices are available to detect the coastline in an easy way using satellite images [20–25].

Furthermore, drones equipped with optical and thermal cameras are increasingly used in environmental surveys. The applications of these sensors on drones are available for the detection of peat fires [26], wildlife detections and monitoring [27,28], building audits, forest monitoring [29], agriculture parameters estimations [30], etc. Due to the general low resolution of thermal images, thermal and optical images can be combined to generate higher-resolution and high-quality thermal mapping models [31,32]. These data, easily acquired by low-cost drones, can also find applications in the definition and monitoring of the coastline.

Several researchers conducted studies for the coastline detection and monitoring using different methods. Zanutta et al. [33] performed 3-D surveys of the coast in the Emilia Romagna region (Northern Italy) using the photogrammetric SfM by drone equipped with optical camera and GNSS (PPK, post-processed kinematics). They demonstrated the ability of these methodologies for coastline monitoring by using 3D digital models extracted from the surveys. However, the authors refer to the 0-level coastline extracted from digital models, but do not investigate the applicability of these methods in the real-time coastline detection. Michałowska et al. [34] used aerial photographs and orthophotomaps over a 65-year time interval for the coastline monitoring of the southern coast of the Baltic Sea (Slowinski National Park) in order to study the erosion and accumulation phenomena. They took advantage of the absence of anthropogenic impact and non-tidal sea with periodic sea level fluctuations. In this case, the authors compared the foredune toe line, the natural line formed by vegetation on the beach obtained on the basis of the visual interpretation of the orthophotomaps. However, with this approach they did not detect the real ground–water separation. Romagnoli et al. [35] analyzed the evolution of the long-term patterns of coastal change of Lipari (Aeolian Islands, Italy) in the last 60 to 70 years using a multidisciplinary approach, which includes aerial photogrammetric images, drone surveys, and satellite

data, high-resolution multi-beam bathymetry and field observations. The authors digitized the coastline from orthomosaics for the multi-temporal comparison without analyzing the aspects linked to the tide level, since the study was focused on the long-term scale.

In the above-mentioned works, the authors focused their analyses on the restitution and comparison of the 0-level coastline, but the real-time ground–water separation was not investigated.

Typically, the restitution of the 0-level contour line can be performed by acquiring high-resolution data (from aerial optical images, LiDAR, GNSS, classical topography, etc.) of the area under investigation in low tide. In this way, after the generation of the 3D model (point cloud) and the Digital Terrain Model (DTM), the automatic 0-level contour line is assumed to represent the estimation of the coastline. On the contrary, the detection of the real-time coastline is a challenge due to several reasons: (i) high tide and low tide real-time contour levels can be extracted from DTMs covering areas below the mean sea level, which may not be available in many cases; (ii) the tidal stations, which provide the tidal elevation, can be far from the area under investigation, making the information related to the tidal data less accurate in the study area or with delays or advances compared to the forecasts. In this context, while the above-mentioned works focused on estimating and monitoring the coastline related to the 0-level contour line, the real-time coastline detection has received limited attention.

This work focuses on the identification of the real-time (instantaneous) coastline, in low tide elevation using high-resolution geomatics techniques. For this aim, the main objective is to analyze the performances of the different techniques in terms of coverage, resolution, and accuracy. In addition to the more commonly used techniques, the extraction of the real-time coastline from thermal imagery by means of a supervised classification method is performed. Data related to the instantaneous coastline are used for the definition of the involved transition surfaces from land to sea, taking advantage of several aims: (i) accurate definition of the free beach area; (ii) boundaries detection of the areas assigned to bathing facilities and/or for fishing-related activities; (iii) strip of surface interested by the periodic water fluctuation (periodically flooded, from low tide to high tide and vice versa) that can be used in the multi-temporal comparisons, etc.

In detail, the real-time detection of the coastline was investigated by means of GNSS RTK (Real-Time Kinematic) measurements, topographic total station, and SfM photogrammetric surveys using a low-cost drone acquiring both optical and thermal images. The test sites were located in the flat area of the Po River Delta (PRD) (an area subject to the phenomenon of land subsidence in northern Italy) [6]. The Boccasette and Barricata beaches were investigated at the beginning of 2022 (Figure 1).

In both cases, the coastline in low tide conditions was surveyed simultaneously with the different techniques, reducing the field work to one hour to avoid different tide elevations in the acquired data. Thermal images were acquired only for a portion of Barricata Beach.

The comparison between the different techniques applied in these sample sites was used to evaluate the accuracy and reliability of the methods. This approach could represent a valid tool for analyzing the multi-temporal evolution of the coastline, which is fundamental for long-term monitoring and risk-mitigation activities in the area.

The procedure followed the subsequent phases (Figure 2):

1. Validation of the GNSS RTK real-time coastlines using the polylines measured with the total station;
2. Extraction of the DTMs and orthophotos from optical and thermal photogrammetric data;
3. Georeferencing and validation of the photogrammetric data;
4. Restitution of the real-time coastlines on the optical and thermal orthophotos;
5. Extraction of the automatic real-time coastline from the thermal orthophoto;

6. Comparison between the reference GNSS RTK polylines with those obtained from the photogrammetric orthophotos, both in terms of distances and surfaces generated by polyline intersections;
7. Evaluation of accuracies and performances of the different techniques;
8. Extraction of the 0-level contour lines from the DTMs;
9. Extraction of the 0-level contour lines from the DTM generated using an ALS (Airborne Laser Scanning) LiDAR survey conducted in 2018;
10. Comparison between the obtained 0-level contour lines to evaluate modifications of the coastlines in terms of erosion and/or accretion in the 2018–2022 period.
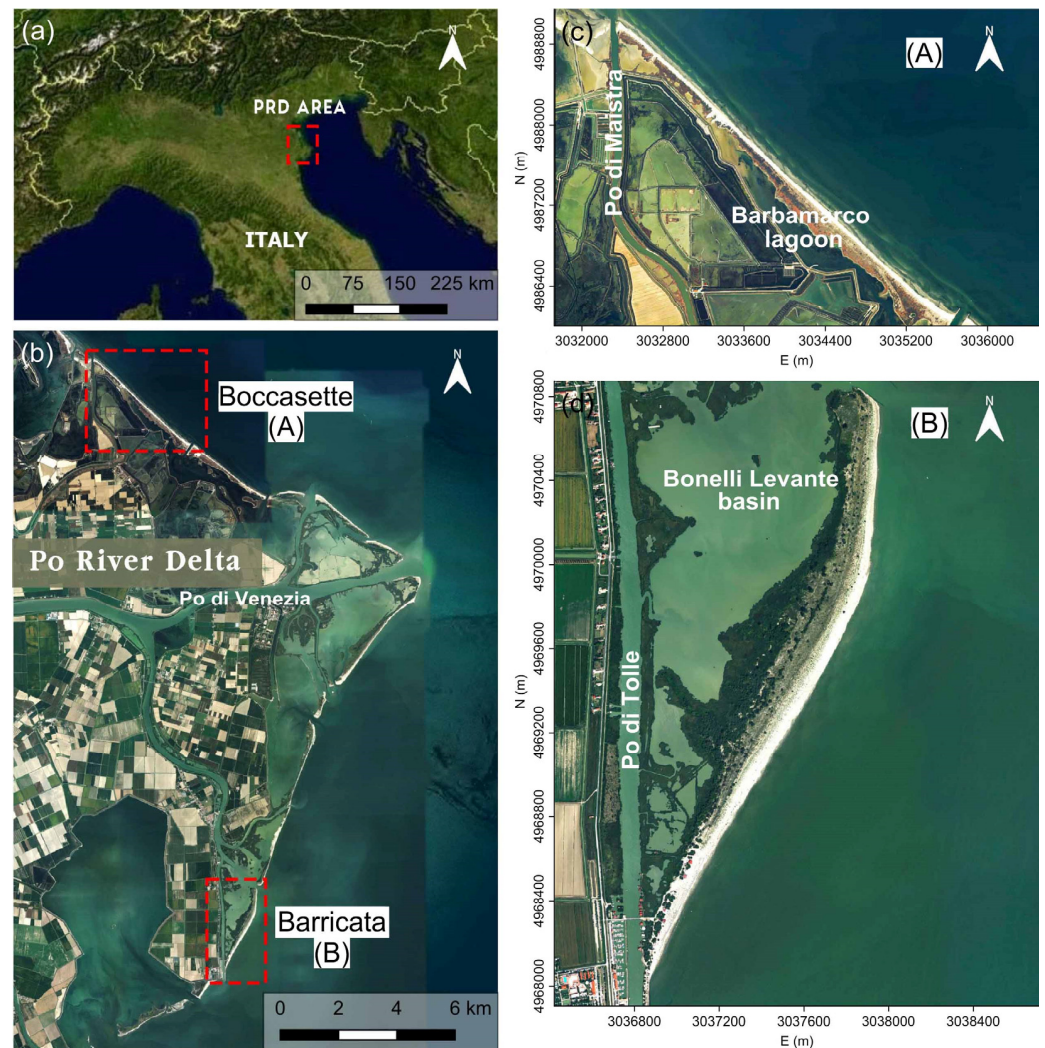

Figure 1. (**a**) Location of the Po River Delta (PRD) in northern Italy; (**b**) location of the studied areas; Boccasette beach (**c**) in the Barbamarco lagoon and Barricata beach (**d**) in the Bonelli Levante basin.

This work is organized as follows. Section 2 introduces the two study areas in the PRD. Section 3 describes the surveys performed using the different techniques, the available LiDAR data collected in 2018, the procedures adopted in the processing, and the approaches used in the coastline comparisons. Section 4 provides the experimental results focusing on real-time and 0-level coastlines multi-temporal comparisons. Section 5 discusses the obtained results, and Section 6 summarizes the work and provides some conclusions.

Figure 2. Flowchart of the methodology proposed in this work.

2. The Study Areas

The coastal areas under investigation, the Boccasette and Barricata beaches, are located in the PRD. It is the last portion of the Po River basin, subdivided into seven branches that flow into the Adriatic Sea. In the past, PRD was affected by high values of land subsidence rates ([14,36,37] and references therein). Currently, the phenomenon, even strongly reduced, is still ongoing [38–40], and most of the area lies below the mean sea level (in the order of 2–3 m), protected by earthen levees for hydraulic safety [41–43].

The Boccasette beach is a flat coastal portion in the northern part of the main branch of the Po River (Po di Venezia). It is characterized by fine sand and extends for about 4.4 km in the southeast-northwest direction, from the northern mouth of the Barbamarco lagoon to the Po di Maistra mouth (Figure 1). Similarly, Barricata beach is a flat coastal portion in the southern part of the Po di Venezia branch: it is characterized by fine sand and extends for about 3.2 km in the north-south direction, from the mouth in the center of the Bonelli Levante basin to the Po di Tolle mouth (Figure 1). Both areas are located outside the embankments, on islets connected to the earthen levees with two bridges. That of Barricata is only open in the summer. Additionally, bathing establishments are active in both areas during the summer, which occupy about 200 m of the beaches around the access bridges.

3. Materials and Methods

3.1. The Surveys

3.1.1. GNSS RTK and Classical Topographic Measurements

The surveys of the coastline were carried out under low tide conditions to reconstruct the morphology of the studied areas below the mean sea level. Information about tide elevation was provided by the Forecasting and Tide Reporting Centre (Centro Previsioni e Segnalazioni Maree) service of the Venice Municipality [44]. Based on these data and considering the delay reported in the PRD, the survey was conducted on 27 January and 25

February 2022 for the Boccasette and Barricata beaches, respectively. Measurements were carried out in winter to avoid interferences with (i) bathing establishments and (ii) other anthropic activities (fishing, and similar) that are mainly active in summer. In addition, due to fact that the motion of waves on flat areas greatly complicate the estimation of the ground–water separation by the operator, the measurements were performed during minimum wind speed, which minimizes the sea waves motion on the beaches, simplifying the operator's choices. The surveys start far from bathing establishments, from the southeastern corner and from the northern corner in the Boccasette and Barricata areas, respectively (Figure 1).

In both cases, taking into account the minimum tide level (−0.5 m at 13:55 for Boccasette and −0.3 m at 13:35 for Barricata), the measurements started half an hour earlier and ended half an hour later (from 13:25 to 14:25 for Boccasette and from 13:05 to 14:05 for Barricata), in order to carry out the survey with the three different techniques in the same tide conditions.

In the GNSS RTK survey a Leica Viva GS 15 GNSS receiver was used. The GNSS antenna was fixed to the operator's backpack by measuring the height from the phase center to the ground (Figure 3a). The sampling rate was set to one second and the operator walked along the ground–sea transition estimating the real-time coastline in the planned hour. A total of 3600 and 3035 points were acquired and distances of 4.78 and 3.99 km were traveled for the Boccasette and Barricata beaches, respectively, with average distance between points of 1.3 m (in the Barricata the survey finished early due to the minor length of the beach). Data were registered in the UTM reference system (EPSG:6876 RDN2008/Zone 12, N-E). At the same time, a total station Leica TCR1201 was used. The station was stationed on a GCP (used for the low-cost drone survey) and oriented to a second GCP for the co-registration of the topographic data in the same reference system of the photogrammetric and GNSS RTK surveys. The measurements were made with a second operator equipped with a prism that walked along the ground–sea border, estimating the real-time coastline and acquiring a point every two steps (Figure 3b). After about 1 h, 278 points were acquired covering 0.644 km in Boccasette and 230 points covering 0.568 km in Barricata (average distance between points of 2.4 m). Subsequently, the ellipsoidal elevations obtained with the GNSS measurements were converted to orthometric elevations using parameters provided by the IGMI (Istituto Geografico Militare Italiano).
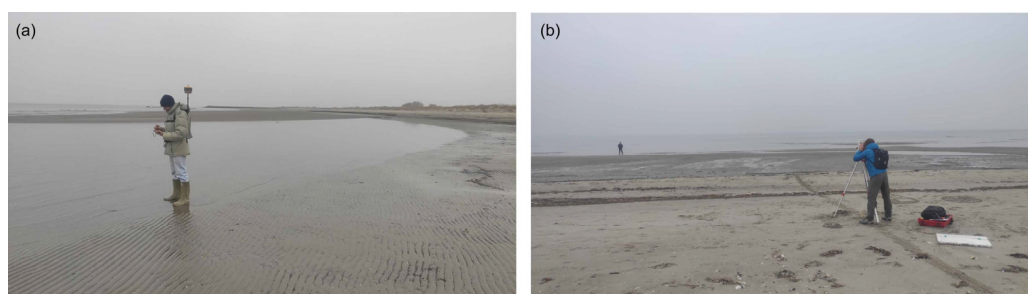

Figure 3. Acquisition of (**a**) real-time kinematic and (**b**) topographic points in the Boccasette area. The photographs highlight the cloudy day, which makes colors uniform (resulting in poor radiometric changes in the optical images) and presents in the ground–water estimation.

3.1.2. The 3D Photogrammetric Survey Using a Low-Cost Drone

During the survey period, a low-cost drone, Parrot Anafi, equipped with an optical camera (Sony IMX230) with a CMOS sensor of 1/2,4″ and diagonal of 7.83 mm, resolution of 21 MP, focal length of 4 mm (equivalent focal of 23 mm, 4608 × 3456 pixels in the image plane), and low-resolution thermal imaging (FLIR camera Lepton 3.5) with 3224 × 2448 pixels in the image plane was used. Before the measurement time, GCPs were uniformly distributed along the investigated areas (Figure 4a); their location was measured using the Leica Viva GS 15 GNSS receiver by applying the RTK approach, co-registering the photogrammetric data in the same reference system of the data acquired with the

other techniques. In detail, 32 and 29 GCPs were measured in Boccasette and Barricata, respectively. In the hour of the measurements, for each investigated area, 4 optical photogrammetric surveys longitudinal to the coast were carried out with an overlap greater than 15% (Figure 4c); each flight was set with an elevation of 60 m, acquiring 6 strips, with each covering 420 m of the longitudinal coast in about 15 min (the runtime of a single battery) and with an overlap between the subsequent images greater than 60% (Figure 4).
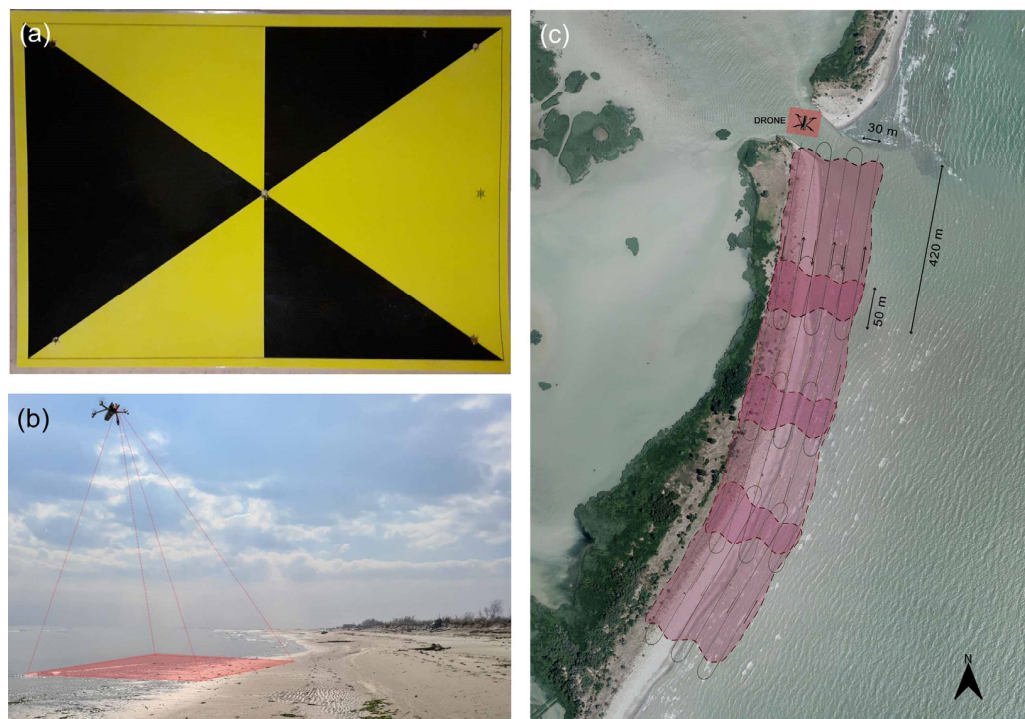
Figure 4. (**a**) SfM (Structure from Motion) photogrammetric targets used during the surveys; (**b**) images acquisition by the low-cost drone; (**c**) covered surface by the four photogrammetric flights in the Barricata area; the image (**b**) highlights the better weather conditions compared to the Boccasette one (Figure 3), featuring a sunny day that improves the colors brightness (resulting in good radiometric changes in the optical images).

Finally, 960 optical images were acquired, covering a surface of about 1.68 × 0.21 km, longitudinal and transversal to the coastline of the Boccasette area. The experience developed on Boccasette beach allowed us to optimize the time in the acquisition of optical images in the Barricata area: for this reason, in addition to 1065 optical images (covering 1.58 × 0.21 km) of the ground–water transition area, a new flight was performed only for Barricata beach during the same hour of survey using the thermal camera. A total of 55 images were acquired in a strip, setting a flight altitude of 110 m and covering an area of about 0.32 × 0.07 km of ground–water separation. The thermal camera on the low-cost drone provided RGB images where the radiometry of each pixel is linked to a scale of temperature (Figure 5). In this way, the performances of the coastline extraction from thermal images can be evaluated.
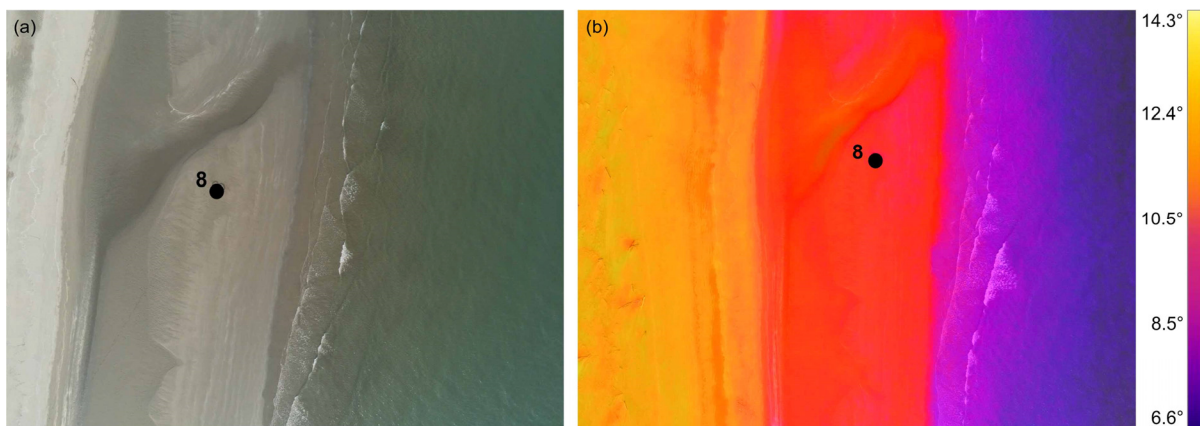
Figure 5. Optical (**a**) and thermal (**b**) images acquired with the low-cost drone, representing the same portion of the Barricata coastal area (around the GCP 8); the acquired coastal portion can be subdivided into three main classes. From left to right: the dry sand, the wet sand, and the sea water. In terms of radiometric changes of the RGB images, the ground–water border is more evident in the thermal image.

3.2. The 2018 LiDAR Data

An ALS LiDAR survey was carried out in the PRD coastal area, outside the levees, on 14 April 2018, using the Optech ALTM Galaxy sensor. These data were available at the Veneto Region (Direzione Pianificazione Territoriale and Unità Organizzativa Genio Civile di Rovigo) and the Local Authority of "Parco Regionale Veneto del Delta del Po". The survey was included in the monitoring activities of the sand islets (where Boccasette and Barricata beaches are located), considerable storm surge barriers that protect the levees from the erosive action generated by the motion of the sea waves. The 3D points were acquired together with ortho-images characterized by GSD (Ground Sample Distance) of 20 cm. Measurements were performed using an integrated GNSS/INS (Inertial Navigation System) system for georeferencing the data during the low tide elevation, so as to cover as much as possible of the ground–sea transition area (using a flight altitude of about 1500 m). Finally, orthometric elevations of the acquired 3D points were obtained from the ellipsoidal one by using the geoid model grids provided by the IGMI. In this way, these data were co-registered in the same reference system of the surveys previously described (Section 3.1.1). In a previous work [14], the 0-level coastline was extracted for the PRD area, including the Boccasette and Barricata case studies (for more details, see Ref. [14]).

3.3. Processing and Comparisons

3.3.1. SfM Photogrammetric Images Processing

The SfM photogrammetric technique was used to generate the 3D point cloud for both Boccasette and Barricata beaches. Agisoft Metashape software version 1.8.4 [45,46] was applied together with the coordinates of the available GCPs to georeference the data. In detail, the GCPs were subdivided in Control Points (CPs, 24 and 22 for Boccasette and Barricata, respectively) used in the processing, and Check Points (ChPs, 8 and 7 for Boccasette and Barricata, respectively) used to evaluate the accuracy of the extracted 3D point clouds [47] (Figure 6).

Subsequently, a DTM and the corresponding orthophoto were generated for both study areas to extract the 0-level contour line, which is assumed to be the real coastline that can be used in the multi-temporal comparisons. The survey in low tide elevation provided clear advantages in the reconstruction of the ground morphology below the mean sea level. Furthermore, the orthophotos were used to generate the temporary coastline (real-time) during the surveys, corresponding to a tide elevation of −0.5 m and −0.3 m in Boccasette and Barricata, respectively. In this case, the restitution of the polylines was performed by

the operator using the visual estimation of the ground–sea boundary, due to the high noise of the automatic contour levels extracted from the DTMs in the ground–water transition.
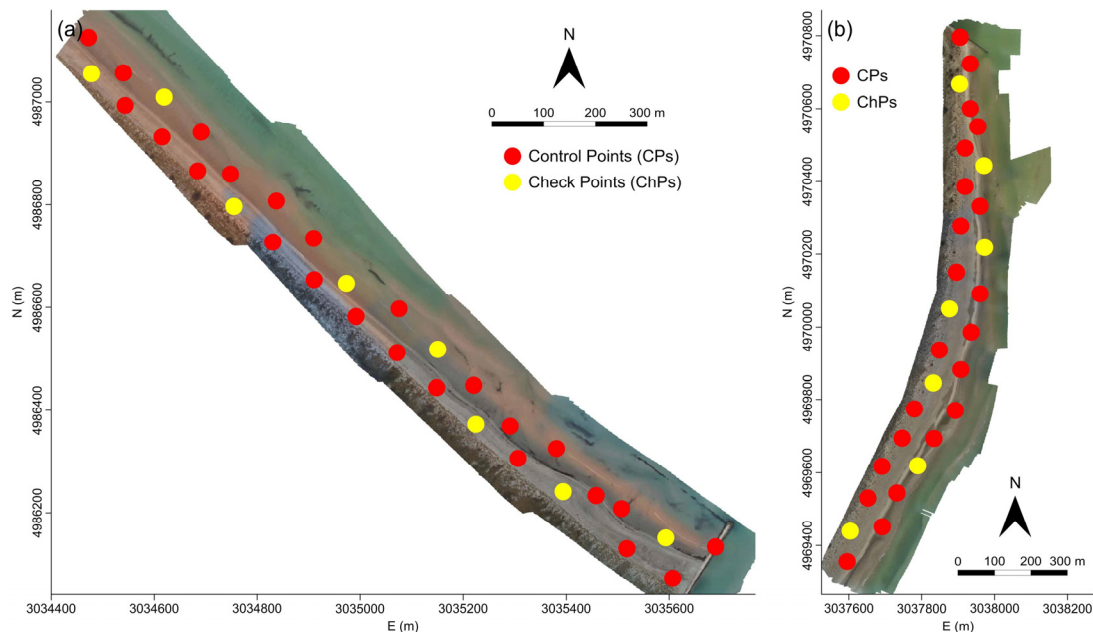

Figure 6. Location of Control Points (CPs) (used in the processing) and Check Points (ChPs) (used to evaluate the accuracy of the extracted 3D models) in the Boccasette (**a**) and Barricata (**b**) beaches.

3.3.2. Automatic Real-Time Coastline Extraction from Thermal Images

In the first phase, because the low-cost drone used in the survey provides the thermal images only in terms of RGB bands, they were used in Agisoft Metashape software version 1.8.4 to extract the orthophoto of the acquired area, which was georeferenced using the available GCPs detectable on the thermal images.

The obtained data were used in the QGIS software version 3.18 to extract the automatic polyline representing the real-time coastline. In this way, a pixel-based classification technique, which includes supervised and unsupervised approaches, was used. In general, supervised classification provides more accurate results, but is time-consuming and requires greater use of resources due to the identification of training samples [48]. On the other hand, supervised classification is commonly adopted in coastline extraction, especially when high-resolution images are used [49]. For this reason, in this work supervised classification was applied to estimate land–water separation. This approach subdivides the spectral range of an image into regions that are linked to a type of land cover. The method requires a priori knowledge of the land cover type to be classified to correctly choose the training samples.

Using the extracted thermal orthophoto, 10 training samples, equally subdivided in terms of the number of pixels, were defined to separate water and ground regions (this procedure was also applied to the optical orthophotos). This way, the orthophotos were transformed into black and white raster images, and the real-time coastlines were extracted based on the separation polyline between the pixels belonging to the two regions.

Subsequently, the polylines were optimized by simplifying the form and eliminating pixel irregularities by introducing new points along the geometry with a step of 2 m (points-to-path algorithm). This value was chosen to align with the order of the coastline estimation, resulting in more regular polylines.

From the thermal orthophoto, the restitution of the real-time coastline was performed by the operator by visual inspection of the land–water boundary.

3.3.3. Coastline Comparisons

The obtained real-time coastlines were compared to each other, both in terms of distances and surfaces generated by polyline intersections. This allowed us to evaluate the following: (i) performances, including accuracies, of the different real-time coastlines generated using the GNSS RTK, total station, manual and automatic restitution on optical and thermal orthophotos with the same tide elevation, in both study areas; (ii) multi-temporal changes using the 0-level contour line derived from the DTMs extracted using the SfM approach (drone DTM 2022) and the ALS LiDAR survey performed in 2018.

In the first series of comparisons, the GNSS RTK coastline was assumed as the ground truth due to the accuracy of this technique and the spatial coverage, which is greater than that of the polylines obtained with the other methods. However, to evaluate the accuracies linked to the land–water estimation by the operator (depending on the sensitivity of the operator in the identification of the coastline), which can be very complex on flat areas influenced by the sea waves motion, the GNSS RTK coastline was compared with the topographic coastline surveyed by other operators in the overlapped areas, in order to validate the GNSS RTK data.

Subsequently, the ground truth GNSS RTK coastline was compared with the following: (i) the restitution on the visible orthophotos; (ii) the restitution on the thermal ortophoto; (iii) the automatic polyline extracted from the thermal orthophoto.

The comparisons were performed by calculating the 2D distances between the obtained polylines in the overlapped areas, providing averages and standard deviations. However, due to the complexity of several portions, which are difficult to evaluate with distances perpendicular to the polylines, the comparisons between the different coastlines were performed by calculating the positive/negative areas of the polygons generated by the polyline intersections. In this study, taking into account the reference GNSS RTK polyline, positive values were obtained in the sea direction, while negative values were attributed in the land direction, both for distances and areas. In the comparison of GNSS RTK and total station polylines using QGIS software version 3.18, perpendicular distances were calculated from the measured topographic points to the GNSS RTK polyline. Areas were calculated considering the polygons generated by the intersection between the GNSS RTK and topographic polylines. The same approach was used when manual and automatic restitutions were involved.

In this case, the uncertainties derived from the comparison between the reference polylines with those obtained by the total station and manual and automatic restitutions were evaluated using the Ratio Index (RI) and the Distributed Ratio Index (DRI) [50]. The first is obtained by dividing the total areas of the generated polygons with the length of the reference GNSS RTK polyline. The latter is calculated by taking into account each obtained polygon, dividing the i-area with the length of the related polyline. This way, statistical parameters such as average and standard deviation can be calculated in order to provide the degree of accuracy.

3.3.4. Accretion/Erosion in the 2018–2022 Period

The multi-temporal comparison involved the contour line of 0-level obtained from the DTMs extracted using the ALS LiDAR measurements performed in 2018 and the photogrammetric surveys carried out with the low-cost drone in 2022. In the first phase, the LiDAR data (in the EPSG: 32632 WGS 84/UTM Zone 32N reference system) were converted into the reference system used in this work.

Similarly to the procedure previously described (Section 3.3.2), starting with the 2018 survey, which is assumed as reference, the comparison was carried out by calculating areas of the polygons generated by the intersection between the multi-temporal coastlines. Accretion (positive) and erosion (negative) were linked to the location of the 2022 coastline compared to the 2018 coastline.

4. Results

4.1. Photogrammetric 3D Models and Orthophotos

Three-dimensional models were generated by means of the SfM approach for Boccasette and Barricata beaches using optical images and the Agisoft Metashape software version 1.8.4. CPs were used in the processing and ChPs were used to validate the 3D models.

Table 1 summarizes the accuracies in terms of RMSE (Root Mean Square Error). The obtained values, in the order of a few centimeters, are in agreement with those reported by Vecchi et al. [9] and Zanutta et al. [33], who worked in similar environmental contexts and with similar settings of photogrammetric surveys using drones.

Table 1. Number of CPs used in processing, available ChPs (see Figure 6), and comparisons between the 3D coordinates and the extracted 3D photogrammetric SfM models in terms of RMSE.

3D Model	N. CPs	N. ChPs	RMSE (cm)	
			CPs	ChPs
Boccasette	24	8	4.1	4.9
Barricata	22	7	3.5	3.8

Subsequently, dense clouds were generated and orthophotos were extracted (Figures 7 and 8).
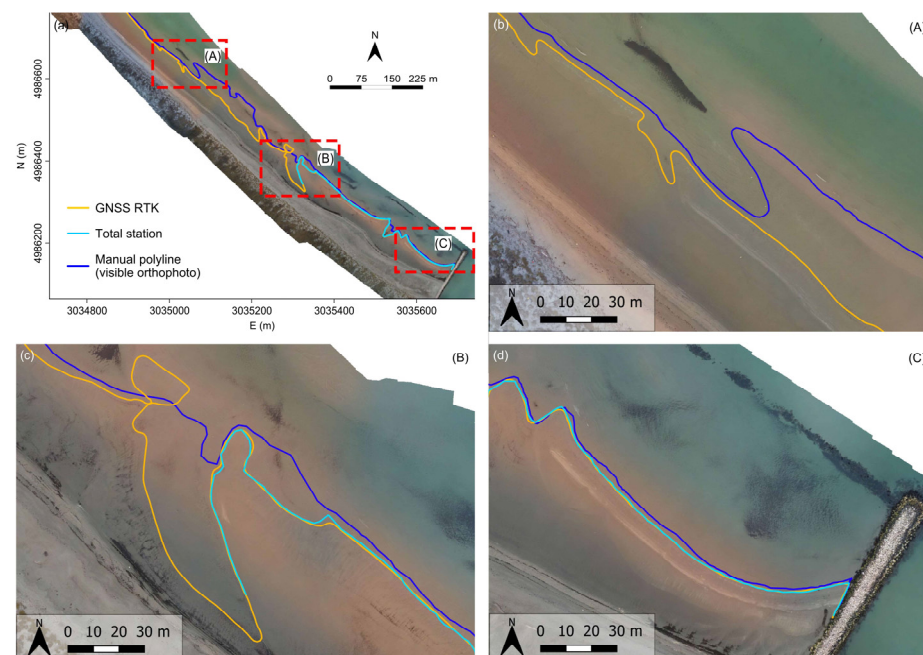
Figure 7. (**a**) Polylines representing the real-time coastlines obtained from the GNSS RTK and topographic surveys and the manual restitution by visual inspection of the optical orthophoto. The background is the same orthophoto of the Boccasette beach; (**b**–**d**) show the three details (A), (B), and (C) respectively.

For a portion of the Barricata beach, a different othophoto was generated using the thermal images. Six CPs were used in the processing based on the available visible targets. The 3D model was extracted with RMSE on CPs of 0.11 m. After the generation of the dense cloud, the corresponding orthophoto was obtained.
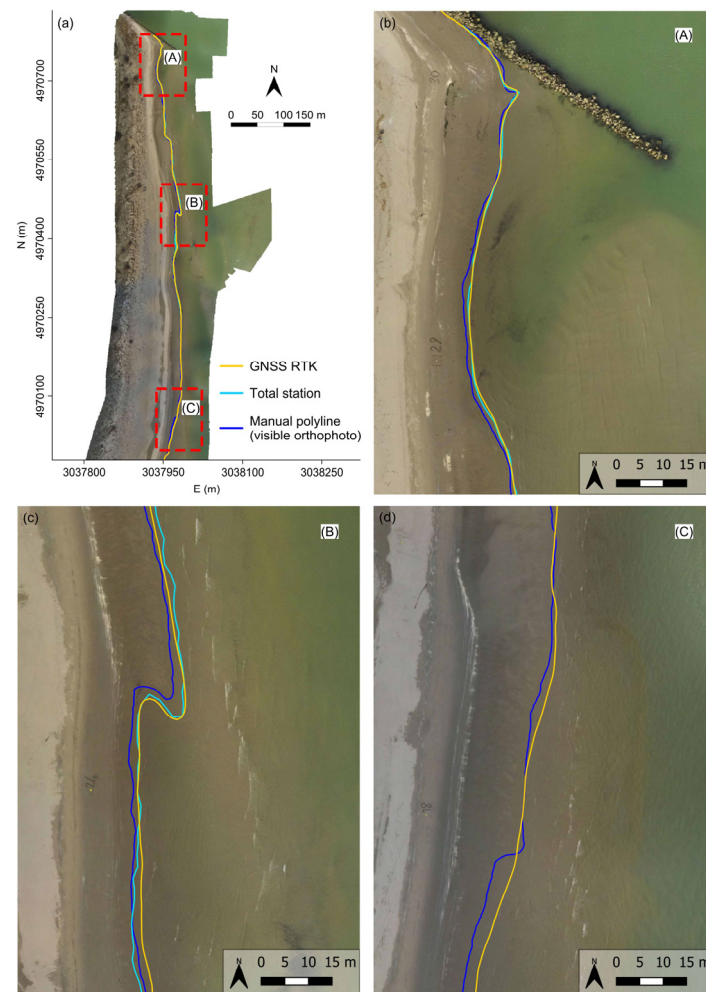
Figure 8. (**a**) Polylines representing the real-time coastlines obtained from the GNSS RTK and topographic surveys and the manual restitution by visual inspection of the optical orthophoto. The background is the same orthophoto of the Barricata beach; (**b**–**d**) show the three details (A), (B), and (C) respectively.

4.2. Restitution of Real-Time Coastlines by Visual Inspection

The restitution of the ground–water polyline separation was performed by the operator using visual inspection. This operation was carried out using both optical (for Boccasette and Barricata) and thermal (only for Barricata) orthophotos. Figures 7 and 8 show the obtained polylines overlapped with the optical orthophotos together with the real-time coastlines obtained with the GNSS RTK and topographic surveys for Boccasette and Barricata, respectively.

Details (A) and (B) of Figure 7b,c show the difficulties of the operator in the interpretation of the ground–water separation from the optical orthophoto with little variation in radiometry of the aerial images (see Figure 3). In these cases, large errors can be performed. On the contrary, details (A), (B), and (C) of Figure 8b–d show that manual restitution of the real-time coastline can provide better results when the bands of the aerial images cover a wide spectrum of the radiometric range.

4.3. Automatic Real-Time Coastline Extraction

Since the low-cost drone used here the thermal imagery from the drone was provided in terms of RGB bands and the land–water separation is radiometrically clearer compared to the optical images (Figure 5), we explored a procedure based on supervised classification to automatically extract the real-time coastline. The availability of only three bands did not

allow us to apply commonly used indexes (for example NDWI, NDVI, etc.) developed for satellite images when other bands are available [20,21].

Figure 9 shows the optical and thermal orthophotos of the Barricata beach overlapped with the polylines generated by means of the following: (i) the GNSS RTK survey; (ii) the manual restitution using visual inspection on both optical and thermal orthophotos; (iii) the automatic polyline extracted from the supervised classification.
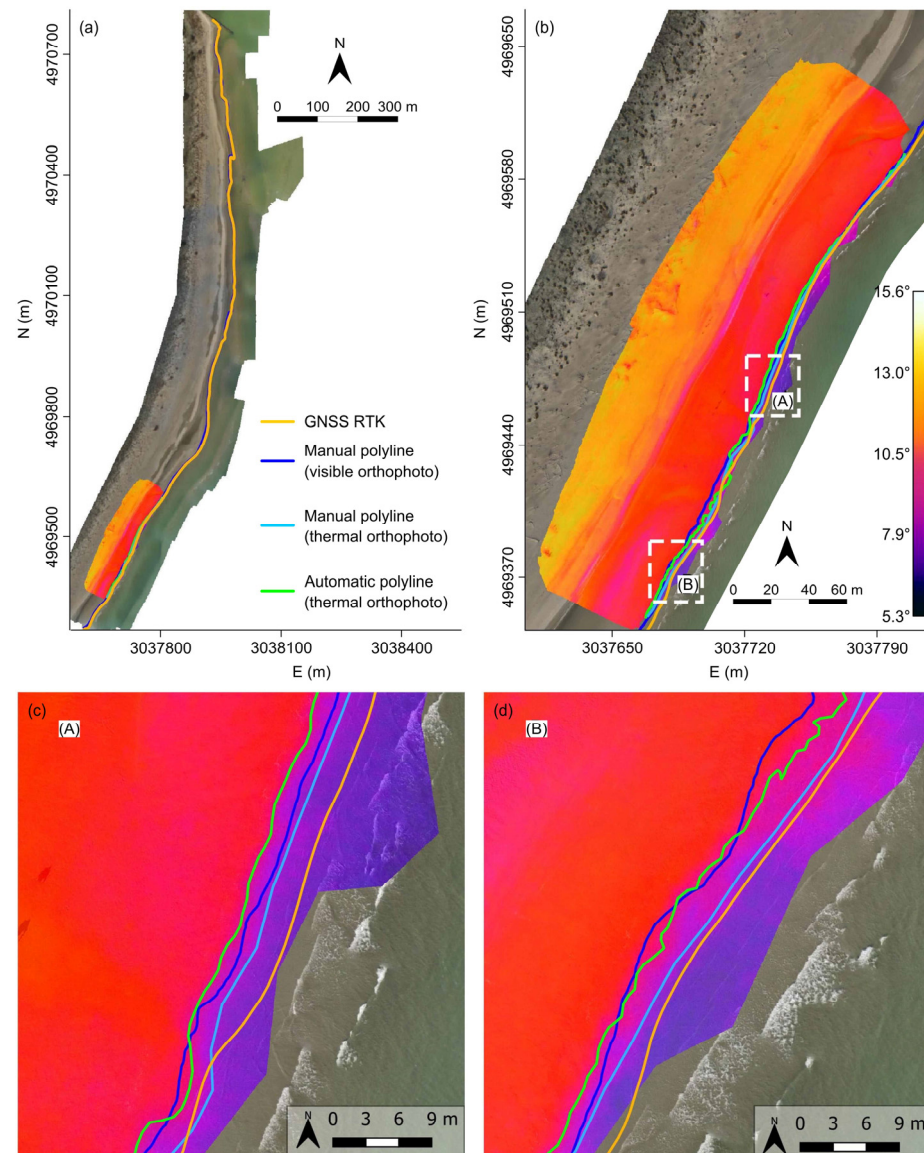

Figure 9. (**a**) Polylines representing the real-time coastlines obtained from the GNSS RTK (i), the manual restitution by visual inspection of the optical (ii) and thermal (iii) orthophotos, the automatic polyline obtained from the supervised classification of the thermal orthophoto (iv). The location of the thermal data on the optical orthophoto of the Barricata beach is also reported; (**b**) detail of the thermal orthophoto; (**c**,**d**) show the two details (A) and (B).

Details (A) and (B) of Figure 9c,d show that all the obtained polylines representing the real-time coastline are very closed, with maximum distances in the order of a few meters.

4.4. Real-Time Coastlines Comparisons

Real-time coastline comparisons were made in terms of distances and surfaces generated by polyline intersections. Figure 10 shows the distance comparisons between the

polylines surveyed with the GNSS RTK technique and the total station topographic instrument, both for the Boccasette and Barricata case studies.
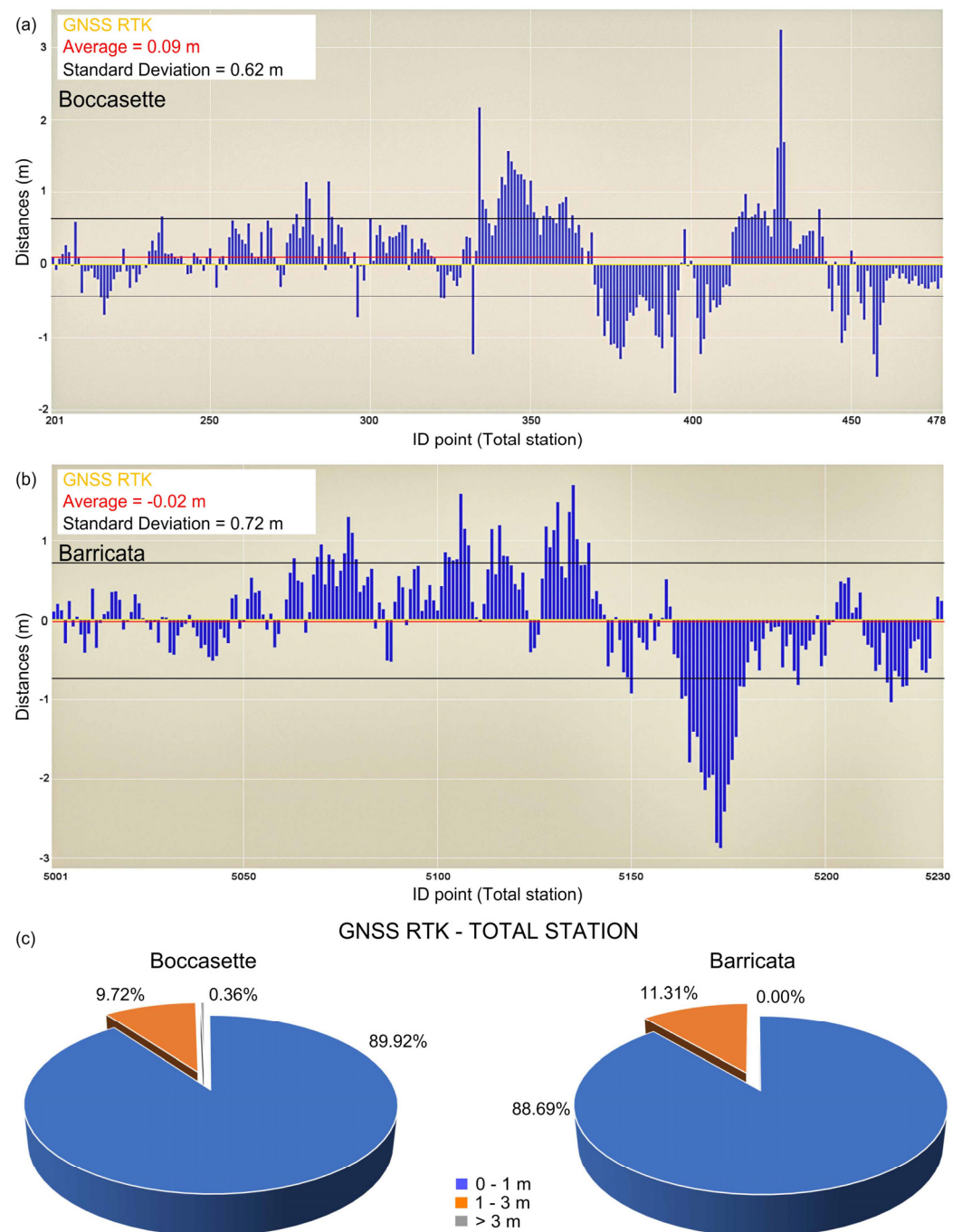

Figure 10. Comparison between GNSS RTK and the total station surveyed polylines representing the real-time coastline both for Boccasette and Barricata beaches: (**a**) distances assuming the GNSS polyline as reference in Boccasette; (**b**) distances assuming the GNSS polyline as reference in Barricata; (**c**) distribution of the calculated distances.

The calculated differences were classified into three groups: (i) less than 1 m; (ii) between 1 and 3 m; and (iii) greater than 3 m. These values were chosen based on the type of the analyzed surfaces (in this case flat areas) and the difficulties in the definition of the real-time coastline due to the motion of waves on the beach. While differences less than 1 m are not significant within the accuracy of the estimation, values between 1 and 3 m can

be acceptable. On the contrary, differences greater than 3 m highlight errors in the detection of the real-time coastline.

The same approach was used in the comparison between the GNSS RTK technique and the polyline extracted by the visual inspection on the orthophotos. Figure 11 shows the obtained results together with the distribution of the distances in the three groups previously defined.
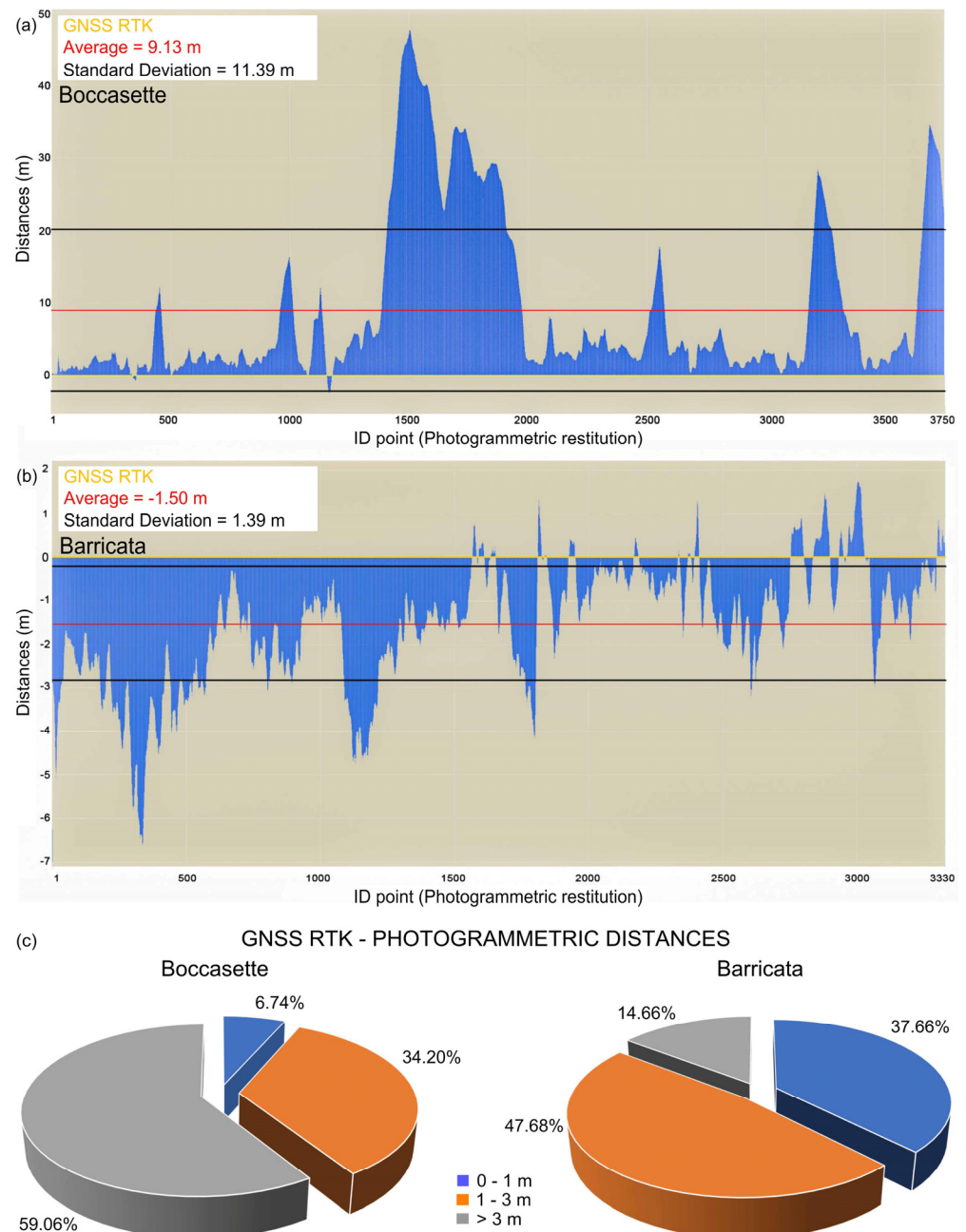

Figure 11. Comparison between GNSS RTK and photogrammetric polyline obtained from visual inspection of the optical orthophoto, representing the real-time coastline both for Boccasette and Barricata beaches: (**a**) distances assuming the GNSS polyline as reference in Boccasette; (**b**) distances assuming the GNSS polyline as reference in Barricata; (**c**) distribution of the calculated distances.

Figure 10a,b show a substantial equilibrium between generated positive and negative distances when the GNSS RTK and the polylines surveyed by the total station are compared, both on the beaches of Boccasette and Barricata. On the contrary, Figure 11a,b show

significant positive distances obtained in Boccasette and negative distances in Barricata, highlighting that the photogrammetric restitution was very different compared to the GNSS RTK measurements.

In addition, in Boccasette 25.7% of the differences provided values greater than 10 m, while in Barricata only 0.01% of the distances provided values greater than 5 m, showing that the SfM technique, together with the restitution by visual inspection on the orthophoto, provided very different results in the two studied areas.

The accuracy of the comparison in terms of surfaces generated by the polyline intersections can be evaluated using the RI and DRI indexes. Tables 2 and 3 show the results obtained for the Boccasette and Barricata case studies.

Table 2. Length, RI, and DRI values derived from the comparison between the GNSS RTK reference polyline with: (i) the survey performed using the total station; (ii) the restitution by visual inspection of the optical orthophoto considering the overlap length with the total station polyline; (iii) the restitution by visual inspection of the optical orthophoto considering the whole dataset for the Boccasette case study.

Comparisons	Length (m)	RI	DRI			
			Min (m)	Max (m)	Average (m)	St. Dev. (m)
GNSS – Total station (i)	635.73	0.47	0.00	0.78	0.21	0.21
GNSS – Restitution (optical) (ii)	635.73	4.67	0.03	6.08	2.63	2.77
GNSS – Restitution (optical) (iii)	2628.52	8.81	0.03	10.60	4.09	3.75

Table 3. Length, RI, and DRI values derived from the comparison between the GNSS RTK reference polyline with: (i) the survey performed using the total station; (ii) the restitution by visual inspection of the optical orthophoto considering the overlap length with the total station polyline; (iii) the restitution by visual inspection of the optical orthophoto considering the whole dataset; (iv) the restitution by visual inspection of the optical orthophoto considering the overlap length with the thermal data; (v) the restitution by visual inspection of the thermal orthophoto; (vi) the automatic polyline extracted from the thermal orthophoto for the Barricata case study.

Comparisons	Length (m)	RI	DRI			
			Min (m)	Max (m)	Average (m)	St. Dev. (m)
GNSS – Total station (i)	563.79	0.52	0.01	0.99	0.22	0.22
GNSS – Restitution (optical) (ii)	563.80	0.93	0.02	1.43	0.46	0.38
GNSS – Restitution (optical) (iii)	1649.78	1.63	0.02	2.41	0.52	0.55
GNSS – Restitution (optical) (iv)	281.30	2.90	-	-	-	-
GNSS – Restitution (thermal) (v)	281.30	1.29	0.22	1.49	0.89	0.56
GNSS – Automatic (thermal) (vi)	281.30	2.76	0.08	3.53	1.18	1.36

4.5. Multi-Temporal Coastlines Comparisons

The comparisons between the 0-level coastline extracted from the ALS LiDAR survey performed in 2018 and the 0-level coastlines extracted using the DTMs obtained from surveys carried out with the low-cost drone in 2022, both for Boccasette and Barricata beaches, are shown in Figure 12.

Polygons generated by the intersection of polylines were classified as erosion (red, when the 2022 drone-based coastline falls in the land direction compared to the 2018 ALS-based coastline) and accretion (green, when the 2022 drone-based coastline falls in the sea direction compared to the 2018 ALS-based coastline).

On Boccasette beach, accretion of 13,751 m^2 was mainly located in the south of the analyzed area where the Barbamarco lagoon opens in the Adriatic Sea. On the contrary, erosion (14,551 m^2) was evident in the northern portion (Figure 12a).
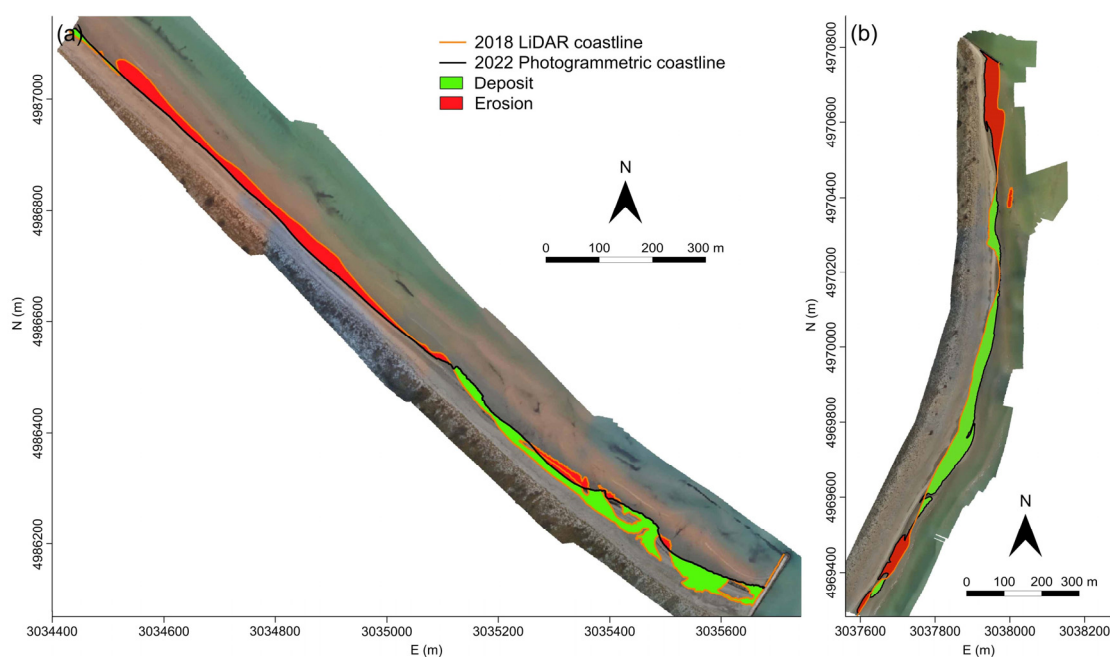
Figure 12. Multi-temporal comparison between the 0-level coastlines obtained from: (i) the survey performed in 2018 (ALS LiDAR); (ii) the DTMs generated using the surveys carried out in 2022 with the low-cost drone applying the SfM approach: (**a**) Boccasette and (**b**) Barricata study areas. The background are the optical orthophotos extracted using the data acquired in 2022.

For Barricata beach, accretion of 21,783 m^2 was detected almost completely in the central portion of the study area, while erosion (14,223 m^2) was located exclusively in the south and, mainly, in the north of the beach, where the Bonelli Levante basin opens into the sea (Figure 12b).

5. Discussion

5.1. Analysis of the Results

The detection of the real-time coastline performed by two operators and using the ground-based GNSS RTK and the total station was very similar, both for Boccasette and Barricata beaches (Figure 10). The differences provided average values of less than 10 cm and standard deviation in the order of 60–70 cm in very challenging areas (Figure 3). For 90% of the points, the differences were less than 1 m in both cases. However, while the GNSS RTK allowed the coverage of 4.78 km for Boccasette and 3.99 km for Barricata within the survey time, the total station had a more limited spatial coverage of 0.64 km and 0.57 km, respectively. For this reason, the GNSS RTK polyline, validated using the total station in the overlapped area, was assumed as the ground truth of the real-time coastline for both study areas.

Involving the restitution performed using visual inspection of the optical orthophotos, the results of the comparison with the GNSS RTK polyline for Boccasette and Barricata were very different. While for Barricata the differences provided an average of 1.5 m and a standard deviation of 1.4 m, these values in Boccasette drastically increased up to 9.1 m and 11.4 m, respectively. Moreover, the points with distances greater than 3 m increased from 15% in Barricata to about 60% in Boccasette (Figure 11). The difficulty in interpreting the land–water boundary by the operator is evident when the radiometry of the optical images presents very small variations (Figure 3). On the contrary, the perception of the land–sea separation is much clearer on sunny days (Figure 4b), where the radiometric changes of the optical images cover a wide range of the spectrum. However, the automatic real-time coastline extracted using the radiometric approach and the supervised classification of the optical orthophotos failed both for Boccasette and Barricata case studies. The radiometric

changes along the ground–water separation were not enough for the automatic detection. This result is in agreement with previous studies conducted in the same areas using aerial photographs. The poor quality of the images increases the errors of manual and automatic restitution of the coastlines [11,14].

In addition, the ground-based GNSS RTK approach is preferable, compared to the drone-based SfM approach, also in terms of costs and spatial coverage, since in the hour of survey with the low-cost drone only 50% of the GNSS RTK polyline was covered.

Similar considerations can be developed by analyzing the RI and DRI indices, when surfaces generated by polyline intersections were generated (Tables 2 and 3). In particular, Table 3 (Barricata case study) shows that the comparison between the GNSS RTK polyline and the restitution by visual inspection on the optical orthophoto related to the same spatial coverage provided RI and DRI values of distance about two times greater than the GNSS RTK and total station comparison. Considering the problems related to the ground–water estimation in these areas, the deterioration of the results was still limited and acceptable for many applications, when the survey was performed in good weather conditions that provided significant radiometric changes of the optical images. On the other hand, the aerial images acquired in bad weather conditions were characterized by poor radiometric changes that provided unacceptable estimation of the coastline (Table 2).

The polyline obtained from the thermal orthophoto provided better results (Table 3). In the overlapped area the RI index was reduced from 2.9 m (GNSS RTK and restitution by visual inspection on the optical orthophoto) to 1.29 m (GNSS RT and restitution by visual inspection on the thermal orthophoto), due to the better radiometric separation of the ground–water boundary on thermal images (Figure 5). The automatic extraction of the real-time coastline slightly improves the results obtained with the optical orthophoto, but with clear advantages of the automatic approach when wide areas must be analyzed.

Considering the promising results of the supervised classification, in future developments the automatic real-time coastline extraction from thermal images will be analyzed more in detail by also using suitable indices developed for multispectral satellite images and adapted to RGB thermal images.

Multi-temporal comparisons of the 0-level contour line in the 2018–2022 period provided general erosion in Boccasette and accretion in Barricata. However, while the calculated erosion in Boccasette was very limited (the average retreat of the coastline was about 0.5 m), in Barricata the accretion was more evident (the average advancement of the coastline was about 4.7 m). The modifications in the analyzed period could be due to several factors such as the dynamics of the nearshore, the morphology of the lagoon behind the two studied beaches, the effects of the storm surges that occurred in the two areas, etc. However, these values are also strongly influenced by both the accuracies of the 3D models and seasonal changes (the ALS LiDAR survey was performed in April 2018 and the photogrammetric SfM surveys were performed in January and February 2022).

5.2. Comparison with Previous Research Works

The results of this work were compared with some others research studies conducted in a similar coastal environment with analogue aims.

Lee et al. [51] performed accuracy and efficiency tests using a total station and a GPS RTK for the measurements of spot points and continuous walking data by means of a backpack system at the Gosapo macro-tidal sand beach (Republic of Korea). They found accuracies of the data in the order of a few centimeters, in agreement with the results obtained in this work regarding the comparison between total station and the GNSS RTK data.

On the other hand, the accuracies of the coastlines obtained from optic and thermal orthophoto were also compared with those estimated by using multispectral satellite images.

Marchel and Specht [52] extracted the coastline at the public beach in Gdynia (Poland) using a DJI Matrice 300 RTK UAV. They generated the Digital Surface Model (DSM) and the orthophotomosaic of the studied area from which the ground–water separation was

extracted. In addition, the authors marked out the coastline course using high-resolution Pléiades Neo satellite imagery (resolution 0.5 m) and Hexagon Europe satellite images (resolution 0.3 m). They calculated the accuracy of the obtained coastlines using a reference polyline measured with a GNSS RTK receiver. The results provided differences of less than 1 m between the UAV and GNSS RTK coastlines. However, this value, which is slightly better than the one obtained in this work, is strongly influenced by the radiometric characteristics of the optic images, depending mostly on the weather conditions and, consequently, the quality of visual inspection.

El Kafrawy et al. [53] compared and evaluated six coastline extraction methods applied to a Landsat8 2015 image related to the Ras El-Hekma (Egypt) coastal zone. They used the reference 2015 coastline extracted from high-resolution imagery of Pléiades B1 (resolution 0.50 m). The results of the comparisons provided by the authors showed 90% of shifting distances in 1 pixel (30 m), highlighting a close correlation between accuracy and pixel size of the satellite images.

Alcaras et al. [50] extracted the coastline of a coastal area close to the delta of the Nestos River, in the Northern Aegean Sea (Easter Macedonia and Thrace, Greece) from very high-resolution (VHR) Pléiades imagery. They extracted the coastline using the Normalized Difference Water Index (NDWI) obtained and processed from both initial images and pan-sharpened images. The authors compared the extracted polyline with the reference one, manually achieved from the panchromatic image. Results of the comparisons provided RI and DRI values comparable with those obtained in this study.

In these last works, the automatic extraction of the coastline was facilitated by the use of multiband satellite images and limited by the ground pixel size [23,50]. On the other hand, with low-cost thermal cameras on drones, the advantage was the acquisition of images with higher resolution, allowing the authors to obtain good results in the automatic coastline extraction—even with only three bands.

6. Conclusions

In this work the detection of the real-time coastline in the flat areas of Boccasette and Barricata beaches (PRD, northern Italy) was investigated. Performances of the GNSS RTK technique, total station topographic instrument, and the photogrammetric SfM approach, using both optical and thermal images acquired with a low-cost drone, were analyzed.

According to the comparisons, the best performances in the detection of the real-time coastline in terms of costs, accuracies, and spatial coverage were obtained using the GNSS RTK technique. Nevertheless, drone-based survey by means of optical and thermal cameras allows for the following: (i) the production of the 3D model of the study area using the optical images, with the extraction of the 0-level contour line, useful in the multi-temporal comparisons; (ii) the real-time coastline detection using automatic procedures based on supervised classification of the thermal images. However, the drone-based survey cannot cover the length of the GNSS RTK measurements in the same working time.

Finally, the ground truth real-time coastline obtained from images using visual inspection or the automatic approach can provide significant errors. This work demonstrated the advantages of the ground-based GNSS RTK survey of the real-time coastline as a reliable ground truth. It can be used as a high-accuracy reference to evaluate the performances of polylines extracted from optical and/or thermal images and acquired from different platforms.

Author Contributions: Conceptualization, M.F.; methodology, M.F., M.B. and M.M.; software, M.F., M.B. and M.M.; validation, M.F., M.B. and M.M.; formal analysis, M.F. and M.B.; investigation, M.F. and M.B.; resources, M.F.; data curation, M.F.; writing—original draft preparation, M.F. and M.B.; writing—review and editing, M.F. and M.M.; visualization, M.F., M.B. and M.M.; supervision, M.F.; project administration, M.F. All authors have read and agreed to the published version of the manuscript.

References

1. Zhao, Q.; Pan, J.; Devlin, A.T.; Tang, M.; Yao, C.; Zamparelli, V.; Falabella, F.; Pepe, A. On the Exploitation of Remote Sensing Technologies for the Monitoring of Coastal and River Delta Regions. *Remote Sens.* **2022**, *14*, 2384. [CrossRef]

2. Ericson, J.P.; Vörösmarty, C.J.; Dingman, S.L.; Ward, L.G.; Meybeck, M. Effective sea-level rise and deltas: Causes of change and human dimension implications. *Glob. Planet. Chang.* **2006**, *50*, 63–82. [CrossRef]

3. Antonioli, F.; Anzidei, M.; Amorosi, A.; Lo Presti, V.; Mastronuzzi, G.; Deiana, G.; De Falco, G.; Fontana, A.; Fontolan, G.; Lisco, S.; et al. Sea-level rise and potential drowning of the Italian coastal plains: Flooding risk scenarios for 2100. *Quat. Sci. Rev.* **2017**, *158*, 29–43. [CrossRef]

4. Kulp, S.A.; Strauss, B.H. New elevation data triple estimates of global vulnerability to sea-level rise and coastal flooding. *Nat. Commun.* **2019**, *10*, 4844. [CrossRef] [PubMed]

5. Karami, E.; Alizadeh, N.; Farhadi, H.; Abdolazimi, H.; Maghsoudi, Y. Monitoring of land surface displacement based on SBAS-InSAR time-series and GIS techniques: A case study over the Shiraz Metropolis, Iran. *ISPRS Ann. Photogramm. Remote Sens. Spatial Inf. Sci* **2023**, *X-4/W1-202*, 371–378. [CrossRef]

6. Fiaschi, S.; Fabris, M.; Floris, M.; Achilli, V. Estimation of land subsidence in deltaic areas through differential SAR interferometry: The Po River Delta case study (Northeast Italy). *Int. J. Remote Sens.* **2018**, *39*, 8724–8745. [CrossRef]

7. Saleh, M.; Becker, M. New estimation of Nile Delta subsidence rates from InSAR and GPS analysis. *Environ. Earth Sci.* **2018**, *78*, 6. [CrossRef]

8. Tang, S.; Song, L.; Wan, S.; Wang, Y.; Jiang, Y.; Liao, J. Long-Time-Series Evolution and Ecological Effects of Coastline Length in Coastal Zone: A Case Study of the Circum-Bohai Coastal Zone, China. *Land* **2022**, *11*, 1291. [CrossRef]

9. Vecchi, E.; Tavasci, L.; De Nigris, N.; Gandolfi, S. GNSS and Photogrammetric UAV Derived Data for Coastal Monitoring: A Case of Study in Emilia-Romagna, Italy. *J. Mar. Sci. Eng.* **2021**, *9*, 1194. [CrossRef]

10. Eboigbe, M.A.; Kidner, D.B.; Thomas, M.; Thomas, N.; Aldwairy, H. Analysis of Low-Cost Uav Photogrammetry Solutions for Beach Modelling and Monitoring Using the Opensource Quantum Gis. In *The International Archives of the Photogrammetry, Remote Sensing and Spatial Information Sciences, Proceedings of the ASPRS 2022 Annual Conference, Denver, CO, USA, 6–8 February and 21–25 March 2022*; ISPRS: Hannover, Germany, 2022; Volume XLVI-M-2-2022.

11. Fabris, M. Coastline evolution of the Po River Delta (Italy) by archival multi-temporal digital photogrammetry. *Geomat. Nat. Hazards Risk* **2019**, *10*, 1007–1027. [CrossRef]

12. Alberico, I.; Cavuoto, G.; Di Fiore, V.; Punzo, M.; Tarallo, D.; Pelosi, N.; Ferraro, L.; Marsella, E. Historical maps and satellite images as tools for shoreline variations and territorial changes assessment: The case study of Volturno Coastal Plain (Southern Italy). *J. Coast. Conserv.* **2017**, *22*, 919–937. [CrossRef]

13. Laksono, F.A.T.; Borzì, L.; Distefano, S.; Di Stefano, A.; Kovács, J. Shoreline Prediction Modelling as a Base Tool for Coastal Management: The Catania Plain Case Study (Italy). *J. Mar. Sci. Eng.* **2022**, *10*, 1988. [CrossRef]

14. Fabris, M. Monitoring the Coastal Changes of the Po River Delta (Northern Italy) since 1911 Using Archival Cartography, Multi-Temporal Aerial Photogrammetry and LiDAR Data: Implications for Coastline Changes in 2100 A.D. *Remote Sens.* **2021**, *13*, 529. [CrossRef]

15. Goksel, C.; Senel, G.; Dogru, A.O. Determination of shoreline change along the Black Sea coast of Istanbul using remote sensing and GIS technology. *Desalination Water Treat.* **2019**, *177*, 242–247. [CrossRef]

16. Viana, R.D; dos Reis, G.N.L.; Velame, V.M.G.; Körting, T.S. Shoreline extraction using unsupervised classification on Sentinel-2 imagery. In Proceedings of the XIX Brazilian Symposium on Remote Sensing, Santos, Brazil, 14–17 April 2019; Volume 19, p. 96606.

17. Alcaras, E.; Amoroso, P.P.; Baiocchi, V.; Falchi, U.; Parente, C. Unsupervised classification based approach for coastline extraction from Sentinel-2 imagery. In Proceedings of the 2021 International Workshop on Metrology for the Sea; Learning to Measure Sea Health Parameters (MetroSea), Virtual Conference, 4–6 October 2021; pp. 423–427.

18. Domazetović, F.; Šiljeg, A.; Marić, I.; Faričić, J.M.; Vassilakis, E.; Panđa, L. Automated Coastline Extraction Using the Very High-Resolution WorldView (WV) Satellite Imagery and Developed Coastline Extraction Tool (CET). *Appl. Sci.* **2021**, *11*, 9482. [CrossRef]

19. Karaman, M. Comparison of thresholding methods for shoreline extraction from Sentinel-2 and Landsat-8 imagery: Extreme Lake Salda, track of Mars on Earth. *J. Environ. Manag.* **2021**, *298*, 113481. [CrossRef] [PubMed]

20. McFeeters, S.K. The use of the Normalized Difference Water Index (NDWI) in the delineation of open water features. *Int. J. Remote Sens.* **1996**, *17*, 1425–1432. [CrossRef]

21. Ma, M.; Wang, X.; Veroustraete, F.; Dong, L. Change in area of Ebinur Lake during the 1998 2005 period. *Int. J. Remote Sens.* **2007**, *28*, 5523–5533. [CrossRef]

22. Wolf, A.F. Using WorldView-2 Vis–NIR Multispectral Imagery to Support Land Mapping and Feature Extraction Using Normalized Difference Index Ratios. In *SPIE 8390, Algorithms and Technologies for Multispectral, Hyperspectral, and Ultraspectral Imagery XVIII, International Society for Optics and Photonics*; SPIE: Bellingham, WA, USA, 2012; Volume 8390, p. 83900N. [CrossRef]

23. Braga, F.; Tosi, L.; Prati, C.; Alberotanza, L. Shoreline detection: Capability of COSMO—SkyMed and high resolution multispectral images. *Eur. J. Remote Sens.* **2013**, *46*, 837–853. [CrossRef]

24. Ma, H.; Guo, S.; Zhou, Y. Detection of Water Area Change Based on Remote Sensing Images. In *GeoInformatics in Resource Management and Sustainable Ecosystem, Communications in Computer and Information Science*; Bian, F., Xie, Y., Cui, X., Zeng, Y., Eds.; Springer: Berlin/Heidelberg, Germany, 2013; Volume 398.

25. Liu, Y.; Wang, X.; Ling, F.; Xu, S.; Wang, C. Analysis of coastline extraction from Landsat-8 OLI imagery. *Water* **2017**, *9*, 816. [CrossRef]

26. Burke, C.; Wich, S.; Kusin, K.; McAree, O.; Harrison, M.E.; Ripoll, B.; Ermiasi, Y.; Mulero-Pázmány, M.; Longmore, S. Thermal-Drones as a Safe and Reliable Method for Detecting Subterranean Peat Fires. *Drones* **2019**, *3*, 23. [CrossRef]

27. Burke, C.; Rashman, M.; Wich, S.; Symons, A.; Theron, C.; Longmore, S. Optimising observing strategies for monitoring animals using drone-mounted thermal infrared cameras. *Int. J. Remote Sens.* **2019**, *40*, 439–467. [CrossRef]

28. Povlsen, P.; Linder, A.C.; Larsen, H.L.; Durdevic, P.; Arroyo, D.O.; Bruhn, D.; Pertoldi, C.; Pagh, S. Using Drones with Thermal Imaging to Estimate Population Counts of European Hare (*Lepus europaeus*) in Denmark. *Drones* **2023**, *7*, 5. [CrossRef]

29. Maurya, N.K.; Tripathi, A.K.; Chauhan, A.; Pandey, P.C.; Lamine, S. Recent Advancement and Role of Drones in Forest Monitoring: Research and Practices. In *Advances in Remote Sensing for Forest Monitoring*; Arellano, P., Pandey, P.C., Eds.; Wiley: Hoboken, NJ, USA, 2022; pp. 223–254.

30. Rouze, G.; Neely, H.; Morgan, C.; Kustas, W.; Wiethorn, M. Evaluating unoccupied aerial systems (UAS) imagery as an alternative tool towards cotton-based management zones. *Precis. Agric.* **2021**, *22*, 1861–1889. [CrossRef]

31. Dahaghin, M.; Samadzadegan, F.; Javan, F.D. Precise 3D extraction of building roofs by fusion of UAV-based thermal and visible images. *Int. J. Remote Sens.* **2021**, *42*, 7002–7030. [CrossRef]

32. Hou, Y.; Chen, M.; Volk, R.; Soibelman, L. Investigation on performance of RGB point cloud and thermal information data fusion for 3D building thermal map modeling using aerial images under different experimental conditions. *J. Build. Eng.* **2022**, *45*, 103380. [CrossRef]

33. Zanutta, A.; Lambertini, A.; Vittuari, L. UAV Photogrammetry and Ground Surveys as a Mapping Tool for Quickly Monitoring Shoreline and Beach Changes. *J. Mar. Sci. Eng.* **2020**, *8*, 52. [CrossRef]

34. Michałowska, K.; Głowienka, E. Multi-Temporal Analysis of Changes of the Southern Part of the Baltic Sea Coast Using Aerial Remote Sensing Data. *Remote Sens.* **2022**, *14*, 1212. [CrossRef]

35. Romagnoli, C.; Bosman, A.; Casalbore, D.; Anzidei, M.; Doumaz, F.; Bonaventura, F.; Meli, M.; Verdirame, C. Coastal Erosion and Flooding Threaten Low-Lying Coastal Tracts at Lipari (Aeolian Islands, Italy). *Remote Sens.* **2022**, *14*, 2960. [CrossRef]

36. Teatini, P.; Tosi, L.; Strozzi, T. Quantitative evidence that compaction of Holocene sediments drives the present land subsidence of the Po Delta, Italy. *J. Geophys. Res.* **2011**, *116*, B08407. [CrossRef]

37. Corbau, C.; Simeoni, U.; Zoccarato, C.; Mantovani, G.; Teatini, P. Coupling land use evolution and subsidence in the Po Delta, Italy: Revising the past occurrence and prospecting the future management challenges. *Sci. Total Environ.* **2019**, *654*, 1196–1208. [CrossRef] [PubMed]

38. Farolfi, G.; Bianchini, S.; Casagli, N. Integration of GNSS and satellite InSAR data: Derivation of fine-scale vertical surface motion maps of Po Plain, Northern Apennines, and Southern Alps, Italy. *IEEE Trans. Geosci. Remote Sens.* **2019**, *57*, 319–328. [CrossRef]

39. Cenni, N.; Fiaschi, S.; Fabris, M. Monitoring of Land Subsidence in the Po River Delta (Northern Italy) Using Geodetic Networks. *Remote Sens.* **2021**, *13*, 1488. [CrossRef]

40. Fabris, M.; Battaglia, M.; Chen, X.; Menin, A.; Monego, M.; Floris, M. An Integrated InSAR and GNSS Approach to Monitor Land Subsidence in the Po River Delta (Italy). *Remote Sens.* **2022**, *14*, 5578. [CrossRef]

41. Carlo, C. Physical Processes and Human Activities in the Evolution of the Po Delta, Italy. *J. Coast. Res.* **1998**, *14*, 775–793.

42. Correggiari, A.; Cattaneo, A.; Trincardi, F. The modern Po Delta system: Lobe switching and asymmetric prodelta growth. *Mar. Geol.* **2005**, *222–223*, 49–74. [CrossRef]

43. Simeoni, U.; Corbau, C. A review of the Delta Po evolution (Italy) related to climatic changes and human impacts. *Geomorphology* **2009**, *107*, 64–71. [CrossRef]

44. Municipality of Venice, Centro Previsioni e Segnalazioni Maree. Available online: https://www.comune.venezia.it/it/content/centro-previsioni-e-segnalazioni-maree (accessed on 24 February 2022).

45. Agisoft LLC. *Agisoft Metashape User Manual*; Professional Edition, Version 1.8; Agisoft LLC: St. Petersburg, Russia, 2022.

46. Agisoft LLC. *Metashape Python Reference, Release 1.8.2*; Agisoft LLC: St. Petersburg, Russia, 2022.

47. Fabris, M.; Fontana Granotto, P.; Monego, M. Expeditious Low-Cost SfM Photogrammetry and a TLS Survey for the Structural Analysis of Illasi Castle (Italy). *Drones* **2023**, *7*, 101. [CrossRef]

48. Nagendra, H.; Gadgil, M. Biodiversity Assessment at Multiple Scales: Linking Remotely Sensed Data with Field Information. *Proc. Natl. Acad. Sci. USA* **1999**, *96*, 9154–9158. [CrossRef]

49. Maglione, P.; Parente, C.; Santamaria, R.; Vallario, A. Modelli Tematici 3D Della Copertura Del Suolo a Partire Da DTM Immagini Telerilevate Ad Alta Risoluzione WorldView-2. *Rend. Online Della Soc. Geol. Ital.* **2014**, *30*, 33–40. [CrossRef]

50. Alcaras, E.; Falchi, U.; Parente, C.; Vallario, A. Accuracy Evaluation for Coastline Extraction from Pléiades Imagery Based on NDWI and IHS Pan-Sharpening Application. *Appl. Geomat.* **2022**, *15*, 595–605. [CrossRef]
51. Lee, J.M.; Park, J.-Y.; Choi, J.-Y. Evaluation of sub-aerial topographic surveying techniques using total station and RTK-GPS for application in macrotidal sand beach environment. *J. Coast. Res.* **2013**, *65*, 535–540. [CrossRef]
52. Marchel, Ł.; Specht, M. Method for Determining Coastline Course Based on Low-Altitude Images Taken by a UAV. *Remote Sens.* **2023**, *15*, 4700. [CrossRef]
53. El Kafrawy, S.; Basiouny, M.; Ghanem, E.; Taha, A. Performance evaluation of shoreline extraction methods based on remote sensing data. *J. Geogr. Environ. Earth Sci. Int.* **2017**, *11*, 1–18. [CrossRef]